Simultaneous Potential and Circuit Solution for Two-Dimensional Bounded Plasma Simulation Codes

Vahid Vahedi and G. DiPeso

Lawrence Livermore National Laboratory, Livermore, California 94551

An algorithm for coupling external circuit elements to be bounded two-dimensional electrostatic plasma simulation codes is developed. In general, the external circuit equations provide a mixture of Dirichlet and Neumann boundary conditions for the Poisson equation, which is solved each time step for the internal plasma potential. We rewrite the coupling between the plasma and the external circuit parameters as an algebraic or ordinary differential equation for the potential on the boundary. This scheme allows decomposition of the field solve into a Laplace solver with boundary conditions (e.g., applied potentials) and a Poisson solver with zero boundary conditions. We present the details of the external circuit coupling to an explicit electrostatic planar two-dimensional particle-in-cell code called PDP2, and discuss briefly how the coupling can be done in an implicit electrostatic code. The decomposition replaces the iterative coupling with a direct coupling and reduces the amount of computational time spent in the field solver. We use PDP2 to simulate a dually excited capacitively coupled RF discharge and show how such a system can be used as a plasma processing tool with separate control over ion flux and ion bombarding energy. © 1997 Academic Press

I. INTRODUCTION

Computer modeling and simulation of bounded plasma devices are now widely used in the plasma processing community [1–6] as well as in the microwave plasma tube community [7]. In most of these models, the domain of the computer experiment includes the entire plasma, dielectric and/or conducting walls, dielectric and/or conducting walls, dielectric and/or conducting internal structures, with the boundary and internal electrodes coupled to external circuits. The addition of external circuits usually places a mixed set of Dirichlet/Neumann boundary conditions on the internal fields. A comprehensive review of the considerations involved in a bounded one-dimensional electrostatic plasma simulation code was presented by Lawson [8] who also included external circuit elements in his analysis. However, Lawson's scheme was first-order accurate and he did not solve the internal field and the external circuit equations simultaneously. Verboncoeur *et al.* [9] showed that in some cases Lawson's external circuit solution was no longer known at the same time as the internal fields.

Verboncoeur *et al.* [9] improved upon Lawson's method and showed how the external circuits can be solved simultaneously with the internal fields. The approach and equations we use in this work for coupling to the external circuits have their roots in the work of Verboncoeur *et al.* [9], and we extend their work to two-dimensional simulations. Even in electromagnetic codes, one has to account for the electrostatic fields resulting from the local charge imbalances [7]. Hence, this scheme may also be used in electromagnetic simulations.

The model we discuss here is a two-dimensional (x, y) bounded electrostatic particle simulation with external circuit elements and an applied uniform or non-uniform magnetic field. Figure 1 shows the system being simulated. The left and right electrodes may be driven separately with voltage or current sources. In case of external voltage sources, the external circuits may also include blocking capacitors to stop the flow of DC currents which would otherwise flow in the external circuit due to the asymmetry. We show the details of the coupling for simple external circuits, and discuss how one may extend the work to more general circuits. Thomas *et al.* [10] have presented a general approach for including lumped circuit elements in a finite difference time domain (FDTD) solution of Maxwell's equations. Their methodology allows a direct access to SPICE for modeling the lumped circuits, while the full 3-dimensional solution to Maxell's equations provides the plasma response. We may also use the same approach for including more general external circuits in our simulations.

We place a rectangular mesh over the system on which the particle charge densities are accumulated in order to solve for the electrostatic field quantities at the mesh points. The charge-gathering and particle-pushing algorithyms used in this model are standard particle-in-cell techniques which can be found in Birdsall and Langdon [11]. Because the ions are typically much heavier than the electrons and hardly move on the electron time-scale, they may be advanced with a much larger time step. This scheme is the essence of subcycling in particle simulations [11–13], which improves the efficiency of multiple-species particle
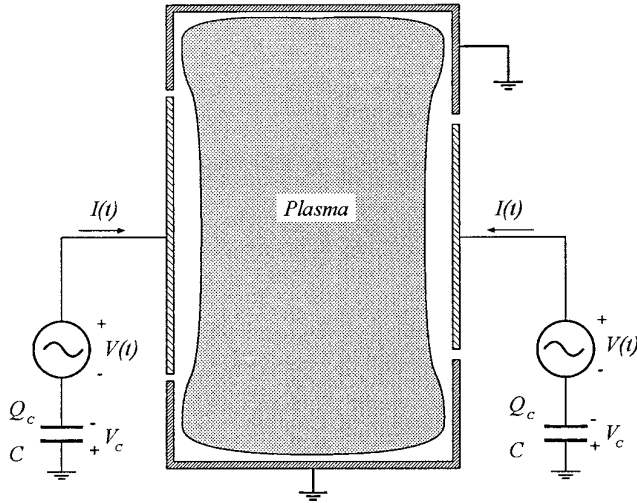
FIG. 1. The two-dimensional simulated system. Top and bottom boundaries are grounded; the left and right electrodes may be the driven by external circuits. The external circuits consists of either a voltage source and a blocking capacitor or a current source.

simulation by making the cost of advancing the ions negligible compared with that of the electrons.

In order to model collisional plasmas and self-sustained discharges, we have added a Monte Carlo collision (MCC) package [14–16], including the null collision method [17, 18], to the usual PIC charged particle scheme, as shown in Fig. 2. The full three-dimensional character of a collision is modeled with three velocity components. For our calculations, the neutral particles are assumed to have a Maxwellian velocity distribution and a uniform density within the boundaries. The model remains valid if the neutral density is a function of position and time.

In this algorithm, we rewrite the coupling between the

plasma and the external circuit parameters as an algebraic or ordinary differential equation for potential on the boundary. This scheme allows us to decompose the field solve into a Laplace solver with boundary conditions due to the external circuit, and a Poisson solver with zero boundary condition. These boundary conditions may be given as Dirichlet (e.g., applied potentials), Neumann (e.g., applied surface charges), or a set of mixed Dirichlet/Neumann (e.g., general external circuit). We present the details of the external circuit coupling to an explicit electrostatic rectangular two-dimensional particle-in-cell code. Note that in explicit electrostatic codes, the Laplace equation is solved only once at the beginning of the simulation in order to determine a normalized internal vacuum field due to the applied boundary conditions. An algebraic equation or an ordinary differential equation is then solved each time step in order to compute the magnitude of the field to scale the vacuum field. The vacuum field is then added to the field obtained from the zero boundary condition Poisson solver in order to obtain the total field inside the plasma. We will also focus on Dirichlet boundary conditions and later discuss the addition of Neumann boundary conditions. Note that the boundary conditions are specified at the walls or internal structures which means that our calculation includes the plasma sheath. The resolution of the plasma sheath has a significant influence on the accuracy of any field solver and this algorithm is no exception. In this paper, we assume that the plasma sheath is sufficiently resolved.

This algorithm is implemented in PDP2 [1, 19], an explicit electrostatic rectangular two-dimensional particle-in-cell code. As an example, we use PDP2 to simulate a dually excited capacitively coupled RF discharge and show how such a system may be used as a plasma processing tool with separate control over ion flux and ion bombarding
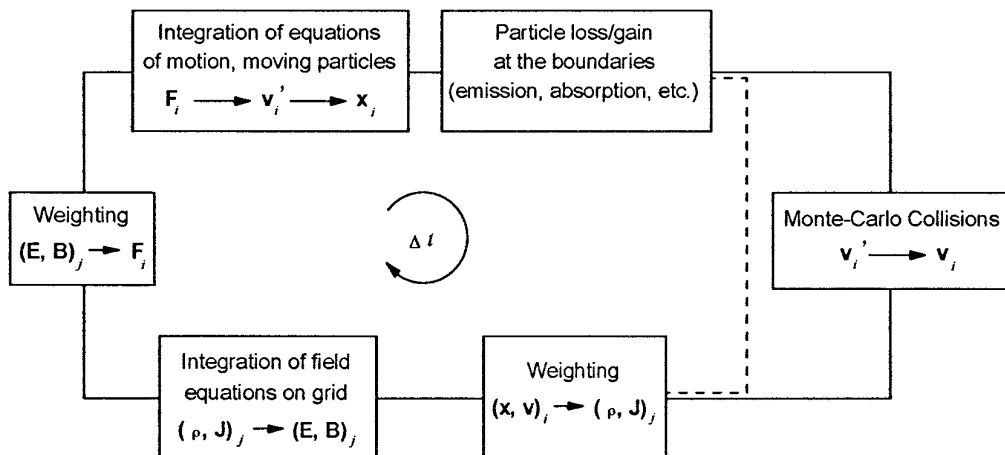

FIG. 2. The flow chart for an explicit PIC scheme with the addition of the Monte Carlo collision package, called PIC-MCC.

energy. For this example we choose a low density plasma ($\sim 10^9$ cm^{-3}) in which we can resolve the RF plasma sheath with a 64 × 64 mesh. The algorithm is still valid at higher plasma densities but requires a finer mesh.

II. ELLIPTIC SOLVER

In order to determine the electrostatic fields in the plasma, we solve the usual explicit form of the Poisson equation for an inhomogeneous system

$$\nabla \cdot [\varepsilon(x, y)\nabla\phi] = -\rho, \tag{1}$$

with the given boundary conditions on all boundaries. In Eq. (1), ϕ is the potential, ρ is the charge density, and $\varepsilon(x, y)$ is the spatially dependent dielectric constant of the medium. If the equations are solved implicitly (e.g., direct implicit particle-in-cell schemes [20]), then we would solve a modified Poisson equation given by [11]

$$\nabla \cdot [(1 + \chi(x, y))\varepsilon(x, y)\nabla\phi] = -\tilde{\rho} \tag{2}$$

where χ is the implicit *numerical* correction to ϕ, and $\tilde{\rho}$ is the charge density from particle motion based only on fields known at the present time step. Inside the plasma, $\varepsilon(x, y) = \varepsilon_0$, and $\varepsilon(x, y)$ enters the problem only for internal dielectrics.

Methods to solve elliptic equations via finite differences are compared and contrasted in Hockney and Eastwood [21]. The methods fall into two general classes: iterative techniques and direct matrix inversions. Among the fastest methods is a direct matrix inversion called cyclic reduction. Unlike Fourier transform methods, cyclic reduction may easily be generalized to cylindrical and spherical coordinate systems. Unfortunately, like Fourier transform methods, cyclic reduction requires that the potential equation be separable. In general, Eqs. (1) and (2) are not separable and cyclic reduction cannot be used. Instead, we choose a more general, but somewhat slower, method to solve Eq. (1) which also preserves the capability of solving Eq. (2). In many models this computational inefficiency is ignorable because the particle moving and weighting takes almost all of a time step.

The Dynamic Alternating Direction Implicit (DADI) method is an iterative technique devised by Doss and Miller [22] that converges rapidly for equations similar to Eqs. (1) and (2) and is our method of choice. According to Doss and Miller, DADI is a factor of 4 slower than a fast direct matrix inversion method for solving Eq. (1) and the directional splitting in the scheme makes DADI easily vectorized for large simulations done on vector computers such as the CRAYs. Hewett, Larson, and Doss [23] applied a variation of the method to solve a coupled set of elliptic equations arising from a reduced version of Maxwell's equations, and their solutions required much less computer time than the biconjugate gradient method previously used.

DADI works as follows. An artificial time dependence is added to convert Eqs. (1) or (2) into a parabolic equation,

$$\partial_{t'}\phi = \nabla \cdot [\varepsilon(x, y)\nabla\phi] + \rho.$$

Then non-iterative ADI is used to advance the "parabolic" equations in time t'. This parabolic equation is then finite-differenced, and a pseudo time step $\Delta t'$ is dynamically adjusted to speed up convergence to the "time" asymptotic state which is the solution of the original elliptic equation. Convergence occurs when the residual of the elliptic equation is less than a chosen tolerance. More detailed explanations may be found in the papers by Doss and Miller [22] and by Hewett, Larson, and Doss [23]. Finally, we add that for parallel computers, the method of choice may be Successive Over Relaxation (SOR) because although DADI takes fewer iterations to achieve a certain residual, the local nature of SOR requires less communication than an ADI sweep.

DADI and other iterative techniques are usually used to solve for steady state problems in which the time derivatives approach zero. We have applied this iterative method to a RF driven plasma in which the solution will approach a cyclic steady state, but the time variation does not go to zero. This means that on average the number of DADI iterations required to converge (to a given accuracy constraint) stays the same every time step in the RF cycle. We will show how superposition and decompositon can reduce the number of iterations each time step in the RF cycle.

III. FINITE DIFFERENCE EQUATIONS ON A UNIFORM MESH

We choose to derive our finite differenced Poisson equation using a Gaussian pillbox on our rectangular mesh instead of finite differencing Eq. (1). The advantage of starting from Gauss' law is that the same equation may then be used to derive boundary conditions on internal and bounding conductive surfaces and internal dielectric structures. Assuming a uniform orthogonal mesh in the (x, y) coordinates, as shown in Fig. 3, Gauss' law at (i, j) may be written as

$$\oint_S \varepsilon\mathbf{E} \cdot \mathbf{dS} = \int_V \rho \, dV + \oint_S \sigma \, dS = Q, \tag{3}$$

or

$$\Delta y \Delta z (\varepsilon_{i+1/2, j}E_{x_{i+1/2, j}} - \varepsilon_{i-1/2, j}E_{x_{i-1/2, j}}) + \Delta x \Delta z$$
$$(\varepsilon_{i, j+1/2}E_{y_{i, j+1/2}} - \varepsilon_{i, j-1/2}E_{y_{i, j-1/2}}) = Q_{ij}, \tag{4}$$
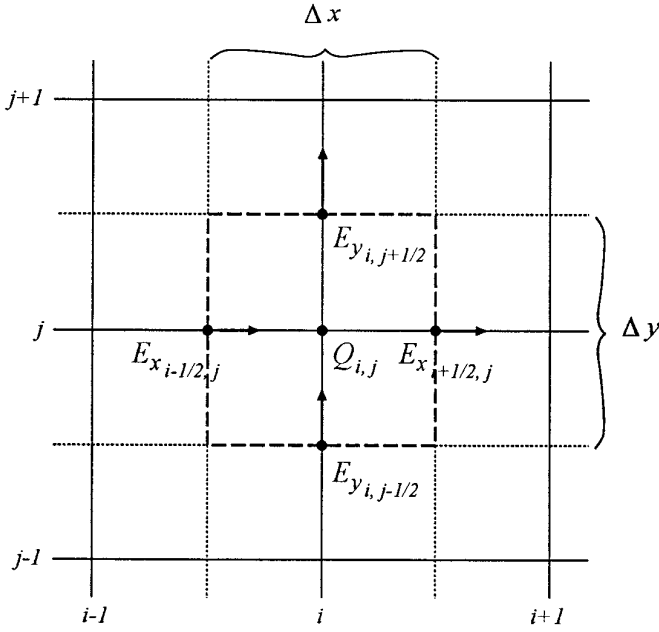
FIG. 3. The Gaussian pillbox, centered at the (i, j) grid point in a system with a uniform mesh, used for the Poisson solver.

where $\varepsilon_{i+1/2,j}$ is the dielectric constant at $(i + 1/2, j)$, Δx and Δy are grid spacings in the x and y directions, Δz is a unit length in the z direction, and Q_{ij} is the total charge at the grid point (i, j). In particle-in-cell codes, Q_{ij} is simply the sum of all charged particles weighted [11] to the grid point (i, j). At a conducting boundary where Eq. (4) is used to determine the normal electric flux, Q_{ij} can be written as

$$Q_{ij} = \rho_{ij}\Delta V_{ij} + \sigma_{ij}\Delta A_{ij}, \qquad (5)$$

where ΔV_{ij} is the volume associated with the grid point (i, j) where free charge exists, and ΔA_{ij} is the area of a physical boundary at (i, j) where surface charge density can accumulate. In Fig. 4, for example, because of the physical structure, the amount of free space volume and physical surface area associated with the grid (i, j) becomes

$$\Delta V_{ij} = \frac{3}{4}\Delta x \Delta y \Delta z \quad \text{and} \quad \Delta A_{ij} = \frac{\Delta z}{2}(\Delta x + \Delta y).$$

At a conducting boundary Eqs. (4) and (5) are solved for σ_{ij} which is equivalent to the normal electric field. In vacuum, $\varepsilon_{ij} = \varepsilon_0$, $\sigma_{ij} = 0$, and $\Delta V_{ij} = \Delta x \Delta y \Delta z$. In electrostatic codes, the electric field is defined as $\mathbf{E} = -\nabla\phi$, or in finite difference form

$$E_{x_{i-1/2,j}} = \frac{\phi_{i-1,j} - \phi_{i,j}}{\Delta x}, \qquad E_{x_{i+1/2,j}} = \frac{\phi_{i,j} - \phi_{i+1,j}}{\Delta x},$$

$$E_{y_{i,j-1/2}} = \frac{\phi_{i,j-1} - \phi_{i,j}}{\Delta y}, \qquad E_{y_{i,j+1/2}} = \frac{\phi_{i,j} - \phi_{i,j+1}}{\Delta y},$$

Substituting the above expressions into Eq. (4), we obtain the finite differenced Poisson equation which can be solved for the potential throughout the system. Note that the above cell centered field expressions are only used to obtain the finite differenced Poisson equation. We use differences over two cells in order to obtain the electric field components for advancing particles [11].

A. Internal Dielectric Objects

Stair step internal dielectrics are included in our system by assigning a dielectric constant to each cell center as shown in Fig. 4. In this case for example, $\varepsilon_{i-1/2,j}$ in Eq. (4) is defined by $\varepsilon_{i-1/2,j} = (\varepsilon_{i-1/2,j+1/2} + \varepsilon_{i-1/2,j-1/2})/2$. The inclusion of internal dielectric structures does not change the size of the unknown ϕ matrix, because the potential inside and on the surface of dielectric structures is not known. If a grid point (i, j) is inside a dielectric or on a free-space dielectric boundary, Eq. (4) is written as an equation for the potential and is incorporated into the finite-differenced matrix. For the grid points inside a dielectric, the source term Q_{ij} is zero, while for the grid points on a free-space dielectric boundary Q_{ij} includes free charges as well as bound charges on the dielectric surface, as shown in Fig. 4. Note that in particle-in-cell codes once a charged particle crosses a boundary into a dielectric, its charge is simply added to the Q's at the grid points terminating the segment crossed by the particle. Hence in Fig. 4, particles $p + 1$ and $p + 2$ at time n contribute to Q_{ij} through the charge density ρ_{ij} (bilinear weighting [11]),
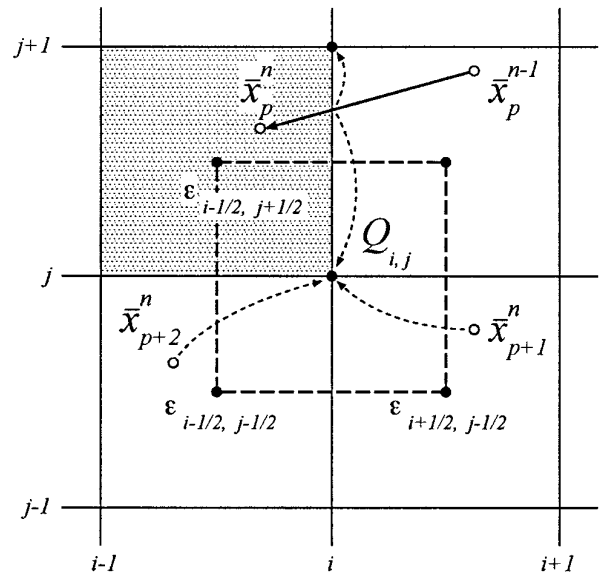

FIG. 4. The Gaussian pillbox, centered at the (i, j) grid point in a system with a uniform mesh. The cell centered at $(i - 1/2, j + 1/2)$ is inside a dielectric while all the other three cells around the grid point (i, j) are vacuum. $\bar{x}_p^n$ is the position of particle p at time n.
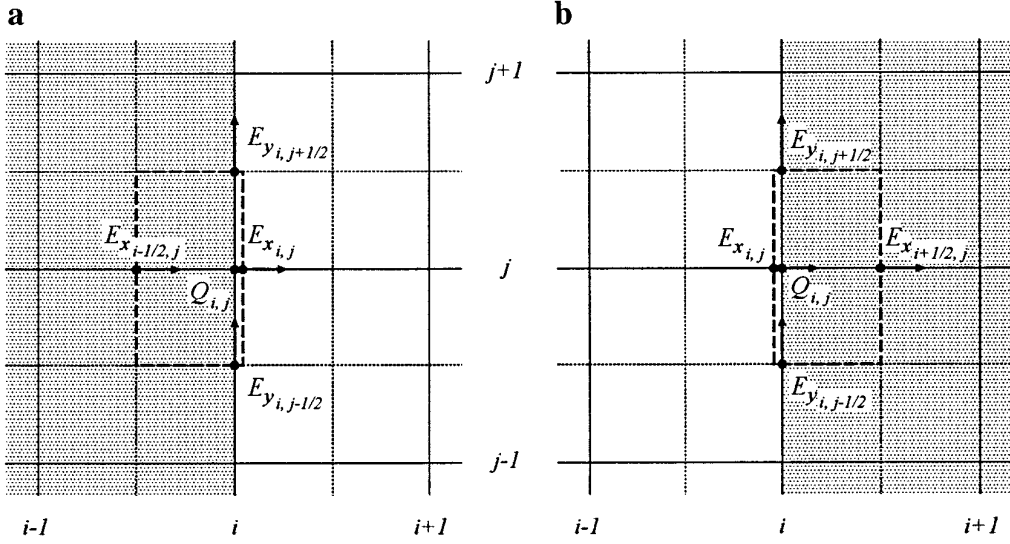
FIG. 5. The Gaussian pillbox, at the (i, j) grid point, a dielectric vacuum boundary. The shaded region is a dielectric.

while particle p contributes to Q_{ij} through the surface charge density ρ_{ij} (bilinear weighting [11]), while particle p contributes to Q_{ij} through the surface charge density σ_{ij} (linear weighting [11]).

After the Poisson equation is solved for the potential using Eq. (4), then we need to solve for the electric field on the mesh points. As noted earlier, the electric field inside a dielectric or in free-space is solved using

$$E_{x_{i,j}} = \frac{\phi_{i-1,j} - \phi_{i+1,j}}{2\Delta x} \quad \text{and} \quad E_{y_{i,j}} = \frac{\phi_{i,j-1} - \phi_{i,j+1}}{2\Delta y}. \quad (6)$$

The fields on the dielectric free-space boundaries, shown in Figs. 5 and 6, are solved using half-size Gaussian pill boxes. The x component of the electric field on the East facing dielectric free-space boundary, as shown in Fig. 5(a), is calculated using

$$\Delta y\Delta z(\varepsilon_{i+1/2,j}E_{x_{i,j}} - \varepsilon_{i-1/2,j}E_{x_{i-1/2,j}})$$
$$+ \frac{\Delta x}{2}\Delta z(\varepsilon_{i-1/2,j+1/2}E_{y_{i,j+1/2}} - \varepsilon_{i-1/2,j-1/2}E_{y_{i,j-1/2}}) = Q_{ij},$$

to be

$$\varepsilon_{i+1/2,j}E_{x_{i,j}} = \frac{Q_{ij}}{\Delta y\Delta z} + \varepsilon_{i-1/2,j}\left(\frac{\phi_{i-1,j} - \phi_{i,j}}{\Delta x}\right) + \frac{\Delta x}{2\Delta y}$$
$$\left[\varepsilon_{i-1/2,j+1/2}\left(\frac{\phi_{i,j+1} - \phi_{i,j}}{\Delta y}\right) - \varepsilon_{i-1/2,j-1/2}\left(\frac{\phi_{i,j} - \phi_{i,j-1}}{\Delta y}\right)\right]. \quad (7)$$

Note that the electric field $E_{x_{i,j}}$ is not calculated at the wall, but infinitesimally away from the wall which is why we use the dielectric constant $\varepsilon_{i+1/2,j}$ instead of $\varepsilon_{i,j}$. The x component of the electric field on the West facing dielectric free-space boundary, as shown in Fig. 5(b), is calculated using

$$\Delta y\Delta z(\varepsilon_{i+1/2,j}E_{x_{i+1/2,j}} - \varepsilon_{i-1/2,j}E_{x_{i,j}})$$
$$+ \frac{\Delta x}{2}\Delta z(\varepsilon_{i+1/2,j+1/2}E_{y_{i,j+1/2}} - \varepsilon_{i+1/2,j-1/2}E_{y_{i,j-1/2}}) = Q_{ij},$$

to be

$$-\varepsilon_{i-1/2,j}E_{x_{i,j}} = \frac{Q_{ij}}{\Delta y\Delta z} + \varepsilon_{i+1/2,j}\left(\frac{\phi_{i+1,j} - \phi_{i,j}}{\Delta x}\right) + \frac{\Delta x}{2\Delta y}$$
$$\left[\varepsilon_{i+1/2,j+1/2}\left(\frac{\phi_{i,j+1} - \phi_{i,j}}{\Delta y}\right) - \varepsilon_{i+1/2,j-1/2}\left(\frac{\phi_{i,j} - \phi_{i,j}}{\Delta y}\right)\right]. \quad (8)$$

The y component of the electric field on the North facing dielectric free-space boundary, as shown in Fig. 6(a), is calculated using

$$\Delta x\Delta z(\varepsilon_{i,j+1/2}E_{y_{i,j}} - \varepsilon_{i,j-1/2}E_{y_{i,j-1/2}})$$
$$+ \frac{\Delta y}{2}\Delta z(\varepsilon_{i+1/2,j-1/2}E_{x_{i+1/2,j}} - \varepsilon_{i-1/2,j-1/2}E_{x_{i-1/2,j}}) = Q_{ij},$$
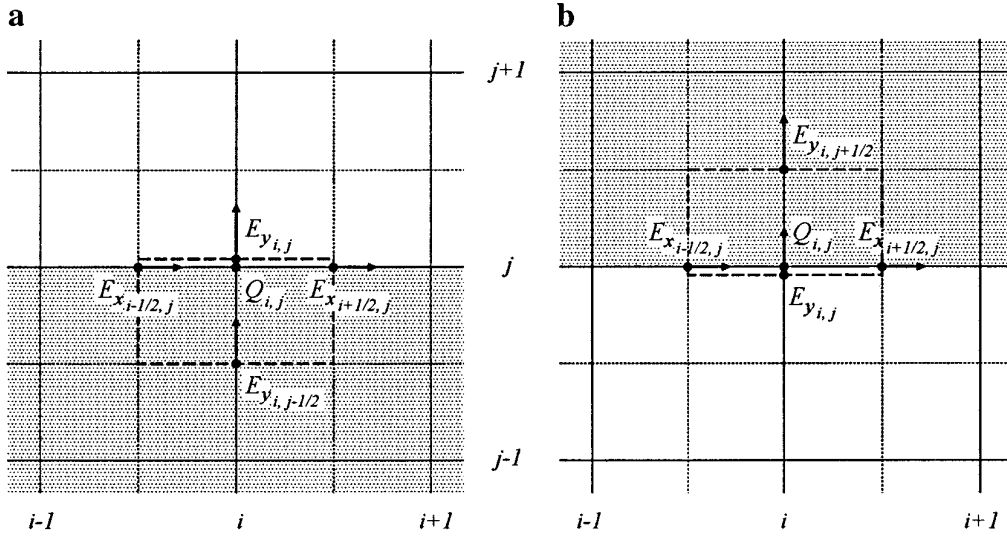
FIG. 6. The Gaussian pillbox, at the (i, j) grid point, a dielectric vacuum boundary. The shaded region is a dielectric.

to be

$$\varepsilon_{i,j+1/2}E_{y_{i,j}} = \frac{Q_{ij}}{\Delta x\Delta z} + \varepsilon_{i,j-1/2}\left(\frac{\phi_{i,j-1} - \phi_{i,j}}{\Delta y}\right) + \frac{\Delta y}{2\Delta x}$$
$$\left[\varepsilon_{i+1/2,j-1/2}\left(\frac{\phi_{i+1,j} - \phi_{i,j}}{\Delta x}\right) - \varepsilon_{i-1/2,j-1/2}\left(\frac{\phi_{i,j} - \phi_{i-1,j}}{\Delta x}\right)\right].$$

(9)

Finally, the y component of the electric field on the South facing dielectric free-space boundary, as shown in Fig. 6(b), is calculated using

$$\Delta x\Delta z(\varepsilon_{i,j+1/2}E_{y_{i,j+1/2}} - \varepsilon_{i,j-1/2}E_{y_{i,j}}) + \frac{\Delta y}{2}\Delta z$$
$$(\varepsilon_{i+1/2,j-1/2}E_{x_{i+1/2,j}} - \varepsilon_{i-1/2,j-1/2}E_{x_{i-1/2,j}}) = Q_{ij},$$

to be

$$-\varepsilon_{i,j-1/2}E_{y_{i,j}} = \frac{Q_{ij}}{\Delta x\Delta z} + \varepsilon_{i,j+1/2}\left(\frac{\phi_{i,j+1} - \phi_{i,j}}{\Delta y}\right) + \frac{\Delta y}{2\Delta x}$$
$$\left[\varepsilon_{i+1/2,j+1/2}\left(\frac{\phi_{i+1,j} - \phi_{i,j}}{\Delta x}\right) - \varepsilon_{i-1/2,j+1/2}\left(\frac{\phi_{i,j} - \phi_{i-1,j}}{\Delta x}\right)\right].$$

(10)

At the inside or outside corner of a dielectric structure no normal can be defined, hence we use Eq. (6) to obtain the electric field components at the corners. Note that Eqs. (7)–(10) reduce to the electrostatic boundary jump

condition, $\varepsilon_1 E_1 - \varepsilon_2 E_2 = \sigma_s$ as $\Delta \to 0$, where σ_s is the surface charge density.

B. Internal Conductors

Our system may also include stair step internal conductors with known DC or time-varying Dirichlet boundary conditions. Unlike the internal dielectric structures, the internal Dirichlet boundary conditions sporadically place known potentials among the unknown potentials in the system which affects our field solver. However, we use the same dynamic ADI field solver with binary masks of 0 or 1 at every grid point for known and unknown potentials. Introducing the binary masks changes some of the coefficients in the matrix solver, but does not increase the computational cost of the dynamic ADI field solver. Once the potential is obtained, we use Eq. (4) to calculate the normal electric field on the conductor vacuum (or conductor dielectric) boundaries.

In order to simplify our discussion and equations in this section and the following sections, we assume that the space immediately surrounding a perfect conductor has the same dielectic constant (i.e., one cell around the conductor $\varepsilon_{ij} = \varepsilon$). Figure 7 shows the different boundary surfaces which might arise in a stair step system. Note that both components of the electric field are zero at points 1–4 in Fig. 7 which implies that the surface charge density σ is identically zero at points 1–4. For all the other points in Fig. 7, either we have a well defined normal electric field which is proportional to the surface charge density, or we define a normal. For example, the normal to the conductor at point 8 in Fig. 7 is in the x-direction, in which case Eqs. (4) and (5) become
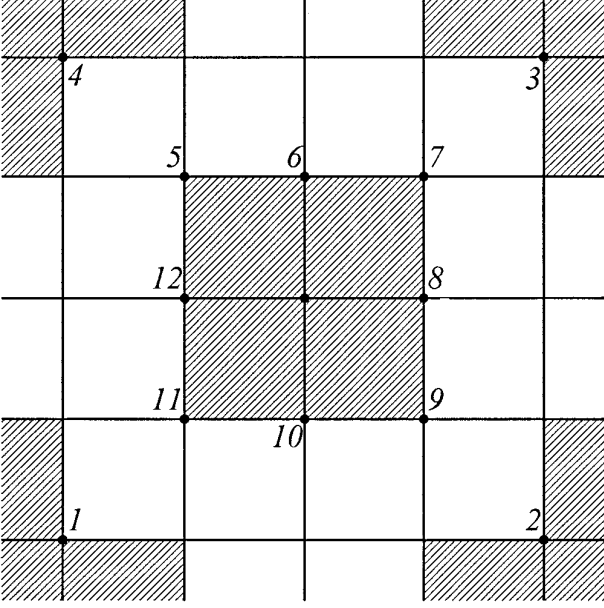
FIG. 7. The shaded region is a perfect conductor bounded by 8 grid points.

$$\varepsilon_{i+1/2,j}E_{x_{i+1/2,j}}\Delta y\Delta z = \rho_{ij}\frac{\Delta x}{2}\Delta y\delta z + \sigma_{ij}\Delta z\Delta y$$

because the fields along and inside a perfect conductor are zero. The above equation is solved for σ_{ij} and along with $E_{x_{ij}}/\varepsilon$ gives the normal electric field at point 8, the surface of a perfect conductor. Rewriting Eq. (4) at each of the grid points 5–12 in Fig. 7 along with the appropriate assumptions about zero fields inside a perfect conductor produces

$$\frac{1}{2}(\Delta x + \Delta y)\frac{\sigma_{ij}}{\varepsilon} = -\frac{3}{4\varepsilon}\Delta x\Delta y\rho_{ij} + \Delta y\left(\frac{\phi_{ij} - \phi_{i-1,j}}{\Delta x}\right)$$
$$+ \Delta x\left(\frac{\phi_{ij} - \phi_{i,j+1}}{\Delta y}\right) \quad (11)$$

$$\frac{\sigma_{ij}}{\varepsilon} = -\frac{1}{2\varepsilon}\Delta y\rho_{ij} + \left(\frac{\phi_{ij} - \phi_{i,j+1}}{\Delta y}\right) \quad (12)$$

$$\frac{1}{2}(\Delta x + \Delta y)\frac{\sigma_{ij}}{\varepsilon} = -\frac{3}{4\varepsilon}\Delta x\Delta y\rho_{ij} + \Delta y\left(\frac{\phi_{ij} - \phi_{i+1,j}}{\Delta x}\right)$$
$$+ \Delta x\left(\frac{\phi_{ij} - \phi_{i,j+1}}{\Delta y}\right) \quad (13)$$

$$\frac{\sigma_{ij}}{\varepsilon} = -\frac{1}{2\varepsilon}\Delta x\rho_{ij} + \left(\frac{\phi_{ij} - \phi_{i+1,j}}{\Delta x}\right) \quad (14)$$

$$\frac{1}{2}(\Delta x + \Delta y)\frac{\sigma_{ij}}{\varepsilon} = -\frac{3}{4\varepsilon}\Delta x\,\Delta y\rho_{ij} + \Delta y\left(\frac{\phi_{ij} - \phi_{i+1,j}}{\Delta x}\right)$$
$$+ \Delta x\left(\frac{\phi_{ij} - \phi_{i,j-1}}{\Delta y}\right) \quad (15)$$

$$\frac{\sigma_{ij}}{\varepsilon} = -\frac{1}{2\varepsilon}\Delta y\rho_{ij} + \left(\frac{\phi_{ij} - \phi_{i,j-1}}{\Delta y}\right) \quad (16)$$

$$\frac{1}{2}(\Delta x + \Delta y)\frac{\sigma_{ij}}{\varepsilon} = -\frac{3}{4\varepsilon}\Delta x\Delta y\rho_{ij} + \Delta y\left(\frac{\phi_{ij} - \phi_{i-1,j}}{\Delta x}\right)$$
$$+ \Delta x\left(\frac{\phi_{ij} - \phi_{i,j-1}}{\Delta y}\right) \quad (17)$$

$$\frac{\sigma_{ij}}{\varepsilon} = -\frac{1}{2\varepsilon}\Delta x\rho_{ij} + \left(\frac{\phi_{ij} - \phi_{i-1,j}}{\Delta x}\right). \quad (18)$$

Equations (11)–(18) are now used at grid points 5–12, respectively, as shown in Fig. 7, on the boundaries and also (as will be shown later) at internal grid points on structures. The electric fields normal to the surface at the grid points 6, 8, 10, and 12 in Fig. 7 are proportional to the charge density σ_{ij} at those grid points and equal to the right hand expression of Eqs. (12), (14), (16), (18). However, strictly speaking, at the grid points 5, 7, 9, and 11, in Fig. 7, the electric field is undefined because one can not define a normal to the surface at those grid points. For those points, we assume that the magnitude of the electric field is proportional to σ_{ij}, while the direction can be approximated by the difference of electric potentials at the adjacent grid points. For example, at grid point 7, we use

$$E_{x_{ij}} = \frac{\sigma_{ij}}{\varepsilon}\left(\frac{E_x}{\sqrt{E_x^2 + E_y^2}}\right), \quad \text{and} \quad E_{y_{ij}} = \frac{\sigma_{ij}}{\varepsilon}\left(\frac{E_y}{\sqrt{E_x^2 + E_y^2}}\right),$$

where σ_{ij} is obtained from Eq. (13), while E_x and E_y are given by

$$E_x = \frac{\phi_{ij} - \phi_{i+1,j}}{\Delta x}, \quad \text{and} \quad E_y = \frac{\phi_{ij} - \phi_{i,j+1}}{\Delta y}.$$

IV. COUPLING TO A SIMPLE EXTERNAL CIRCUIT WITHOUT DECOMPOSITION

In this section we discuss the addition of external lumped circuit elements to the field solver through a boundary condition for a perfectly conducting wall. The boundary of the model is shown in Fig. 8. We assume that the top and bottom boundaries at $j = 0$ and $J = N_y$ are continuous perfectly conducting boundaries, while the side boundaries at $x = 0$ and $x = N_x$ are divided into five segments as shown in Fig. 8. The first and last segments (i.e., $0 < j < N_1$ and $N_4 < j < N_y$) are assumed to be grounded perfect conductors, while the segment $N_2 < j < N_3$ is assumed to be a perfect conductor attached to an external circuit. The potential along the segments $N_1 < j < N_2$ and $N_3 < j < N_4$ is assumed to drop linearly along y which is a reasonable assumption if a dielectric spacer separates the driven electrode from the grounded walls. Here we assume that the spacer is a vacuum gap with the relative dielectric of 1
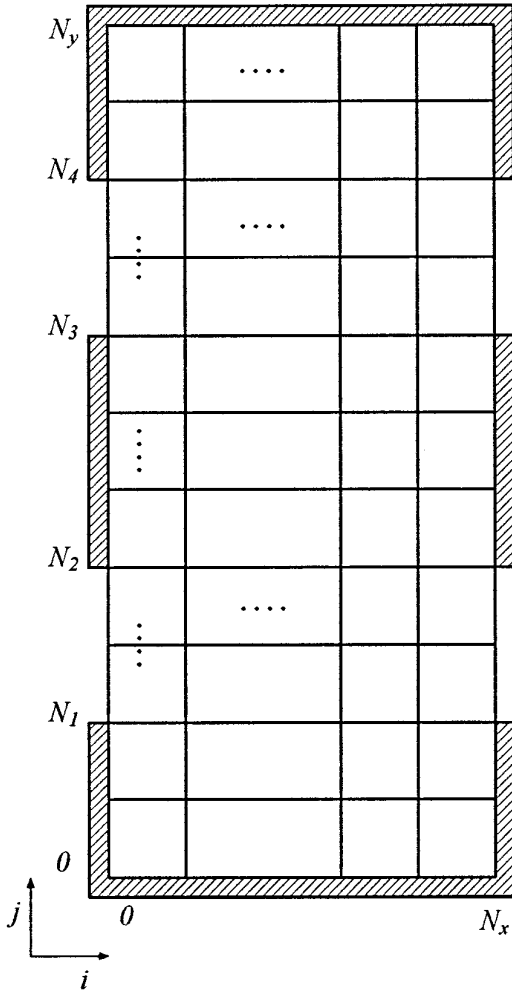
FIG. 8. The two-dimensional system is shown with a uniform mesh. We assume that the boundaries at $j = 0$ and $j = N_y$ are assumed to be continuous perfectly conducting boundaries while the boundaries at $x = 0$ and $x = N_x$ are divided into five segments. The first and last segments (i.e., $0 < j < N_1$ and $N_4 < j < N_y$) are assumed to be grounded perfect conductors, while the segment $N_2 < j < N_3$ is assumed to be a perfect conductor attached to an external circuit. The potential along the segments $N_1 < j < N_2$ and $N_3 < j < N_4$ is assumed to vary linearly which is a reasonable assumption if a spacer separates the driven electrode from the grounded walls.

and no space charge. The linear drop assumption in the gap gives

$$\phi_{0,N_2-1} = \frac{g-1}{g}\phi_{0,N_2} = \frac{g-1}{g}\phi_0 \quad \text{and} \quad \phi_{0,N_3+1} = \frac{g-1}{g}\phi_0,$$
(19)

where g is the number of cells in the gap and is assumed to be at least one because the grounded and driven electrodes should not touch each other. Note that since the driven

electrode is assumed to be a perfect conductor (an equipotential), we only have one unknown on the boundary, i.e.,

$$\phi_{0j} = \phi_0, \qquad N_2 \leq j \leq N_3.$$
(20)

Applying Eqs. (13)–(15) to the left hand side we obtain

$$\sigma_{0j} = \frac{2\varepsilon\Delta y}{\Delta x(\Delta x + \Delta y)}(\phi_{0j} - \phi_{1j})$$

$$+ \frac{2\varepsilon\Delta x}{\Delta y(\Delta x + \Delta y)}(\phi_{0j} - \phi_{0,j-1}) - \frac{3}{2}\frac{\Delta x\Delta y}{\Delta x + \Delta y}\rho_{0j},$$

$$j = N_2$$

$$\sigma_{0j} = \frac{\varepsilon}{\Delta x}(\phi_{0j} - \phi_{1j}) - \rho_{0j}\frac{\Delta x}{2}, \qquad N_2 < j < N_3$$

$$\sigma_{0j} = \frac{2\varepsilon\Delta y}{\Delta x(\Delta x + \Delta y)}(\phi_{0j} - \phi_{1j})$$

$$+ \frac{2\varepsilon\Delta x}{\Delta y(\Delta x + \Delta y)}(\phi_{0j} - \phi_{0,j+1}) - \frac{3}{2}\frac{\Delta x\Delta y}{\Delta x + \Delta y}\rho_{0j},$$

$$j = N_3.$$

We present the implementation of these equations for the left hand side only, but it will become clear how one may add similar equations for the right hand side. We may now couple the boundary conditions in Eq. (21) at the perfect conductor with the external circuit equations at the left side.

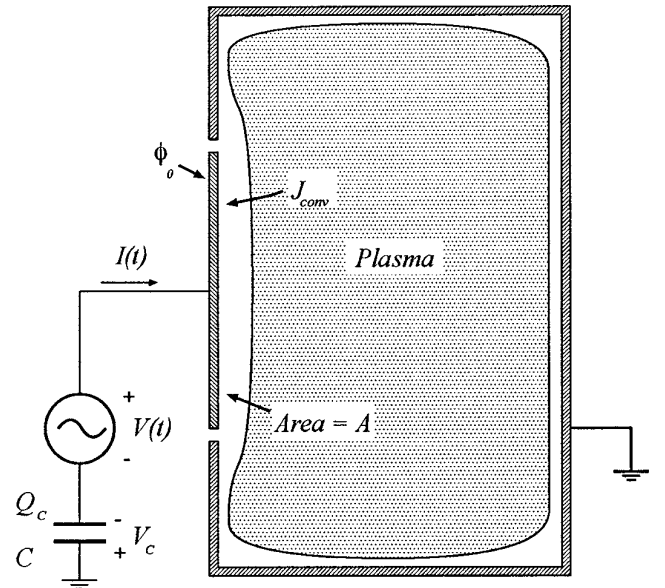Figure 9 shows a simple external circuit consisting of a

FIG. 9. The two-dimensional system to be simulated. All the boundaries are grounded except for part of the left boundary, which is the driven electrode. The external circuit consists of a voltage source and a blocking capacitor which stops the flow of average (DC) current.

voltage source in series with a capacitor coupled to the left electrode. The voltage drop V_c across the capacitor in the external circuit is given by the Kirchhoff's voltage loop law,

$$V_c = V(t) - \phi_0, \qquad (22)$$

where the signs are consistent with the voltage polarities shown in Fig. 9. $V(t)$ is the applied voltage source, and ϕ_0 is the potential on the conductor, as defined in Eq. (20). The time variation of σ_T, the total charge density on the driven electrode, may be obtained from the Kirchhoff's current loop law,

$$A \frac{d\sigma_T}{dt} = I(t) + AJ_{conv}, \qquad (23)$$

where $I(t)$ is the external circuit current, shown in Fig. 9, A is the area of the electrode, and J_{conv} is the convective (conduction) current density arriving at the driven electrode due to plasma charged particles. The discrete finite differenced form of Eq. (23) can be expressed as

$$A(\sigma_T^t - \sigma_T^{t-1}) = Q_c^t - Q_c^{t-1} + Q_{conv}^t, \qquad (24)$$

where $\int dtI = Q_c = CV_c$ is the charge on the capacitor and Q_{conv}^t is the charge deposited on the electrode from the plasma during the time interval $(t - 1, t)$. Combining Eqs. (22) and (24) we find

$$\sigma_T^t = \sigma_T^{t-1} + \frac{1}{A}(CV(t) - C\phi_0^t - Q_c^{t-1} + Q_{conv}^t). \qquad (25)$$

The total charge density σ_T may be expressed by

$$\sigma_T^t = \sum_{j=N_2}^{N_3} \sigma_{0j}^t,$$

where σ_{0j} is defined in Eq. (21) at each grid point j on the driven electrode. Summing over all the equations in Eq. (21) we obtain

$$\sigma_T^t = \frac{\varepsilon}{\Delta x}\left(N + 2\frac{\Delta y - \Delta x}{\Delta y + \Delta x 1} + \frac{4(\Delta x)^2}{g\Delta y(\Delta x + \Delta y)}\right)\phi_0^t$$

$$- \frac{\varepsilon}{\Delta x}\left[\sum_{N_2}^{N_3}\phi_1^t + \frac{\Delta y - \Delta x}{\Delta y + \Delta x}(\phi_{1N_3}^t + \phi_{1N_2}^t)\right] \qquad (26)$$

$$- \frac{\Delta x}{2}\sum_{N_2}^{N_3}\rho_{0j} + \frac{\Delta x(\Delta x - 2\Delta y)}{2(\Delta x + \Delta y)}(\rho_{0N_3} + \rho_{0N_2}),$$

where $N = N_3 - N_2 + 1$, and all the ϕ and ρ terms are obtained at time t. Equations (25) and (26) can be combined and solved for ϕ_0^t to produce

$$\phi_0^t = \frac{\begin{array}{c}\sigma_T^{t-1} + (1/A)(CV(t) - Q_c^{t-1} + Q_{conv}^t) \\ + a + b\phi_{1N_2}^t + c\phi_{1N_3}^t + (\varepsilon/\Delta x)\sum_{N_2}^{N_3}\phi_{1j}^t\end{array}}{d + C/A}, \qquad (27)$$

where

$$a = \frac{\Delta x}{2}\sum_{N_2}^{N_3}\rho_{0j} - \frac{\Delta x(\Delta x - 2\Delta y)}{2(\Delta x + \Delta y)}(\rho_{0N_2} + \rho_{0N_3}),$$

$$b = c = \frac{\varepsilon}{\Delta x}\frac{\Delta y - \Delta x}{\Delta y + \Delta x},$$

and

$$d = \frac{\varepsilon}{\Delta x}\left[N + 2\frac{\Delta y - \Delta x}{\Delta y + \Delta x} + \frac{4(\Delta x)^2}{g\Delta y(\Delta x + \Delta y)}\right].$$

After the potential ϕ_0 on the electrode is obtained from Eq. (27), the total charge density σ_T can be calculated from Eq. (26), and the external circuit parameters can be computed as

$$Q_c^t = A(\sigma_T^t - \sigma_T^{t-1}) + Q_c^{t-1} - Q_{conv}^t \qquad (28)$$

and

$$I(t) = \frac{Q_c^t - Q_c^{t-1}}{\Delta t}. \qquad (29)$$

Note that Eq. (27) is the boundary condition for the Poisson equation. However, because the right hand side of Eq. (27) also contains ϕ_{1j} terms, we must iterate the Poisson equation and the boundary conditions for both to come to equilibrium. This iterative process may be computationally expensive and we recommend the use of superposition of Laplace and Poisson solutions to solve directly for the potential on the boundary.

V. COUPLING TO A SIMPLE EXTERNAL CIRCUIT WITH DECOMPOSITION

An alternate approach to Section IV is to apply superposition and decompose the field solver into the Poisson equation with zero boundary condition and the Laplace equation with the external circuit and other boundary conditions. Note that the decomposition scheme described here is not an approximation. Using this superposition we

will derive an equation exactly equivalent to Eq. (27) but computationally more efficient. The Poisson equation, $\nabla^2\phi_P = -\rho/\varepsilon$ with zero boundary conditions is still solved every time step to account for the space charge effects. Fortunately, the Laplace equation $\nabla^2\phi_{NL} = 0$ need only be solved once to account for the vacuum field effects. Given the length of the driven equipotential electrode, we solve the Laplace equation with $\phi = 1$ on the driven electrode to obtain the boundary effects and the potential profile throughout the system. The potential in the system is then

$$\phi_{ij}^t = \phi_{P_{ij}}^t + \phi_0^t \phi_{NL_{ij}}, \qquad (30)$$

where $\phi_{NL_{ij}} = \phi_{L_{ij}}^t / \phi_0^t$ is the time-independent (one volt) potential profile obtained from solving the Normalized Laplace equation. The potential profiles $\phi_{P_{ij}}^t$ and $\phi_{NL_{ij}}$ are known at time t without having ϕ_0^t. The potential ϕ_0^t on the driven electrode can now be obtained through the decomposition without any iterations. We solve the Poisson equation at time t with zero boundary conditions to obtain $\phi_{P_{ij}}^t$. Then using Eq. (30) we obtain

$$\phi_{1j}^t = \phi_{P_{1j}}^t + \phi_0^t \phi_{NL_{1j}},$$

for $N_2 \le j \le N_3$. Substituting the above form of ϕ_{1j}^t into Eq. (27) and solving for ϕ_0^t produces

$$\phi_0^t = \frac{\sigma_T^{t-1} + (1/A)(CV(t) - Q_c^{t-1} + Q_{conv}^t) + a + b\phi_{P_{1N_2}}^t + c\phi_{P_{1N_3}}^t + (\varepsilon/\Delta x)\sum_{N_2}^{N_3}\phi_{P_{1j}}^t}{d + C/A - b\phi_{NL_{1N_2}}^t - c\phi_{NL_{1N_3}}^t - (\varepsilon/\Delta x)\sum_{N_2}^{N_3}\phi_{NL_{1j}}^t}, \qquad (31)$$

where a, b, c, and d are defined below Eq. (27). Once the potential ϕ_0^t on the electrode is known, the external circuit parameters can be calculated from Eqs. (28) and (29).

VI. OTHER TYPES OF EXTERNAL CIRCUITS

A. Current Source

If the external circuit is a simple current source, then Eq. (23) can be finite differenced as

$$\sigma_T^t = \sigma_T^{t-1} + \frac{1}{A}(I(t)\Delta t + Q_{conv}^t). \qquad (32)$$

Using the superposition approach discussed in the previous section, Eq. (31) may be rewritten as

$$\phi_0^t = \frac{\sigma_T^{t-1} + (1/A)(I(t)\Delta t + Q_{conv}^t) + a + b\phi_{P_{1N_2}}^t + c\phi_{P_{1N_3}}^t + (\varepsilon/\Delta x)\sum_{N_2}^{N_3}\phi_{P_{1j}}^t}{d - b\phi_{NL_{1N_2}}^t - c\phi_{NL_{1N_3}}^t - (\varepsilon/\Delta x)\sum_{N_2}^{N_3}\phi_{NL_{1j}}^t}, \qquad (33)$$

where a, b, c, and d are defined below Eq. (27).

Note that the right hand sides of Eqs. (31) and (33) are known at time t and no iteration is needed.

B. General Circuit

The two examples worked out here were for a simple current source and a simple voltage source external circuits. Verboncoeur *et al.* [9] showed how more general expressions may be finite differenced and coupled as boundary conditions to a internal field solver. In our scheme, we can replace Eqs. (22) and (23) with expressions for more general circuits or simply incorporate Verboncoeur's general circuit expression for Eq. (22). We can also use Thomas' more general approach [10] of coupling to SPICE for including lumped circuit elements in the external circuit.

So far we have discussed the left boundary condition only. It is clear that if both left and right (or other) boundary conditions are applied, one may decompose the field solve into two (or more) Laplace equations and a Poisson equation. If other internal boundary conditions are also applied, then in general the same decomposition can be carried out.

Our discussion above was mainly focused on driven and grounded electrodes and external boundaries (Dirichlet boundary condition). Internal dielectrics may float to a self-consistent potential. However, if we need to impose floating boundary conditions on the external boundaries, then we need to apply a Neumann boundary condition to that boundary. If both Neumann and Dirichlet boundary conditions are applied to the system, the same boundary conditions must be used on each surface for the Poisson equation as well as for the Laplace equations. For example, in the case of a plasma in a bounded box with voltage or current sources applied to biased electrodes, all the boundary conditions may be expressed as Dirichlet type, which makes the decomposition very simple. However, if one were to model a semi-infinite plasma over a biased electrode, Dirichlet boundary conditions would be applied on three sides and a Neumann boundary condition on the remaining boundary in order to represent a semi-infinite plasma.

VII. DECOMPOSITION IN AN IMPLICIT CODE

An implicit Poisson equation may be written to avoid the $\omega_{pe}\Delta t > 2.0$ numerical instability constraint of explicit

codes [11, 24–27]. Although implicit methods have accuracy constraints such as $v_{te}\Delta t/\Delta x < 1$ [27, 28], an order of magnitude increase in Δt is possible for certain problems.

The implicit Poisson equation (ignoring internal dielectrics for simplicity) is given by

$$\nabla \cdot [(1 + \chi(x, y))\nabla \phi] = -\tilde{\rho}. \tag{34}$$

The numerical correction χ is proportional to the pre-push charge density $\tilde{\rho}$ [11, 24–27]. χ is a numerical factor that is time dependent. If there are no external magnetic fields (i.e., χ is a scalar), then the elliptic solver described in Section II applies to this equation. With slight modifications, the finite difference equations of Section III also apply.

With the χ term modifications to Eq. (4) and similar modifications to equations in Section V, Eq. (27) becomes

$$\phi_0^t =$$

$$\frac{\sigma_T^{t-1} + (1/A)(CV(t) - Q_c^{t-1} + Q_{conv}^t) + \tilde{a} + \tilde{b}\,\phi_{1N_2}^t + \tilde{c}\,\phi_{1N_3}^t + (\varepsilon/\Delta x)\sum_{N_2}^{N_3}(1 + (\chi_{0j} + \chi_{1j})/2))\,\phi_{1j}^t}{\tilde{d} + C/A}, \tag{35}$$

where

$$\tilde{a} = \frac{\Delta x}{2}\sum_{N_2}^{N_3}\tilde{\rho}_{0j} - \frac{\Delta x(\Delta x - 2\Delta y)}{2(\Delta x + \Delta y)}(\tilde{\rho}_{0N_2} + \tilde{\rho}_{0N_3}),$$

$$\tilde{b} = \frac{\varepsilon}{\Delta x}\frac{\Delta y - \Delta x}{\Delta y + \Delta x}\left[1 + \frac{\chi_{0N_2} + \chi_{1N_2}}{2}\right],$$

$$\tilde{c} = \frac{\varepsilon}{\Delta x}\frac{\Delta y - \Delta x}{\Delta y + \Delta x}\left[1 + \frac{\chi_{0N_3}}{2}\right],$$

and

$$\tilde{d} = \frac{\varepsilon}{\Delta x}\left[\sum_{N_2}^{N_3}\left(1 + \frac{\chi_{0j} + \chi_{1j}}{2}\right) + \frac{\Delta y - \Delta x}{\Delta y + \Delta x}\right.$$
$$\left(2 + \frac{\chi_{0N_2} + \chi_{1N_2}}{2} + \frac{\chi_{0N_3} + \chi_{1N_3}}{2}\right)$$
$$+ \frac{2(\Delta x)^2}{g\Delta y(\Delta x + \Delta y)}$$
$$\left.\left(2 + \frac{\chi_{0N_2} + \chi_{0N_2-1}}{2} + \frac{\chi_{0N_3} + \chi_{0N_3+1}}{2}\right)\right].$$

Because χ and $\tilde{\rho}$ are pre-push quantities, the electric field E^t and hence ϕ_0^t need not be known to calculate the coefficients a, b, c, and d in Eq. (35). Furthermore, if we derive Q_{conv} from pre-pushed particles that hit the electrode, then ϕ_0^t depends only on ϕ_{1j}^t ($N_2 \leq j \leq N_3$). Hence iteration may once again be avoided by superposition.

Using the same superposition as in Eq. (30), we can decompose Eq. (34), which is linear in ϕ, into an implicit Poisson equation $\nabla \cdot [(1 + \chi(x, y))\nabla \phi_P] = -\tilde{\rho}$ with zero boundary conditions and an implicit Laplace equation $\nabla \cdot [(1 + \chi(x, y))\nabla \phi_{NL}] = 0$ with $\phi_{NL} = 1$ on the given boundary as before. In the explicit scheme, the normalized Laplace equation needed to be solved only once, and scaled each time step. In the implicit scheme, however, because of the time-dependence of the χ term, ϕ_{NL}^t must be solved each time step. Thus, the penalty charged for superposition is one additional Poisson solve, which is a lesser burden than the several Poisson solves required for an iterative ϕ_0 solution. Then using Eq. (30) we obtain

$$\phi_{1j}^t = \phi_{P_{1j}}^t + \phi_0^t\phi_{NL_{1j}}^t,$$

for $N_2 \leq j \leq N_3$, where $\phi_{P_{1j}}^t$ and $\phi_{NL_{1j}}^t$ can again be found without knowing ϕ_0^t. Substituting the above form of ϕ_{1j}^t into Eq. (35) produces

$$\phi_0^t =$$

$$\frac{\sigma_T^{t-1} + (1/A)(CV(t) - Q_c^{t-1} + Q_{conv}^t) + \tilde{a} + \tilde{b}\,\phi_{P_{1N_2}}^t + \tilde{c}\,\phi_{P_{1N_3}}^t + (\varepsilon/\Delta x)\sum_{N_2}^{N_3}(1 + (\chi_{0j} + \chi_{1j})/2))\,\phi_{P_{1j}}^t}{\tilde{d} + C/A - b\,\phi_{NL_{1N_2}}^t - c\,\phi_{NL_{1N_3}}^t - (\varepsilon/\Delta x)\sum_{N_2}^{N_3}(1 + (\chi_{0j} + \chi_{1j})/2)\,\phi_{NL_{1j}}^t}, \tag{36}$$

where the coefficients $\tilde{a}$, $\tilde{b}$, $\tilde{c}$, and $\tilde{d}$, are defined below Eq. (35).

VIII. DUALLY DRIVEN RF DISCHARGES

The algorithm above has been implemented in the code PDP2 [1, 19] and is used to model a dually excited capacitively coupled RF system. The majority of conventional RF plasma processing units are powered by 13.56 MHz RF generators. By treating the excitation frequency as one of the process parameters, we may accomplish accurate and independent control of ion flux and ion bombarding energy. This can be achieved by driving the source and target electrodes with separate power sources. Goto *et al.* [29] investigated the influence of the excitation frequency in a parallel cathode-coupling dually excited system, and found that the self-bias voltage of the cathode became
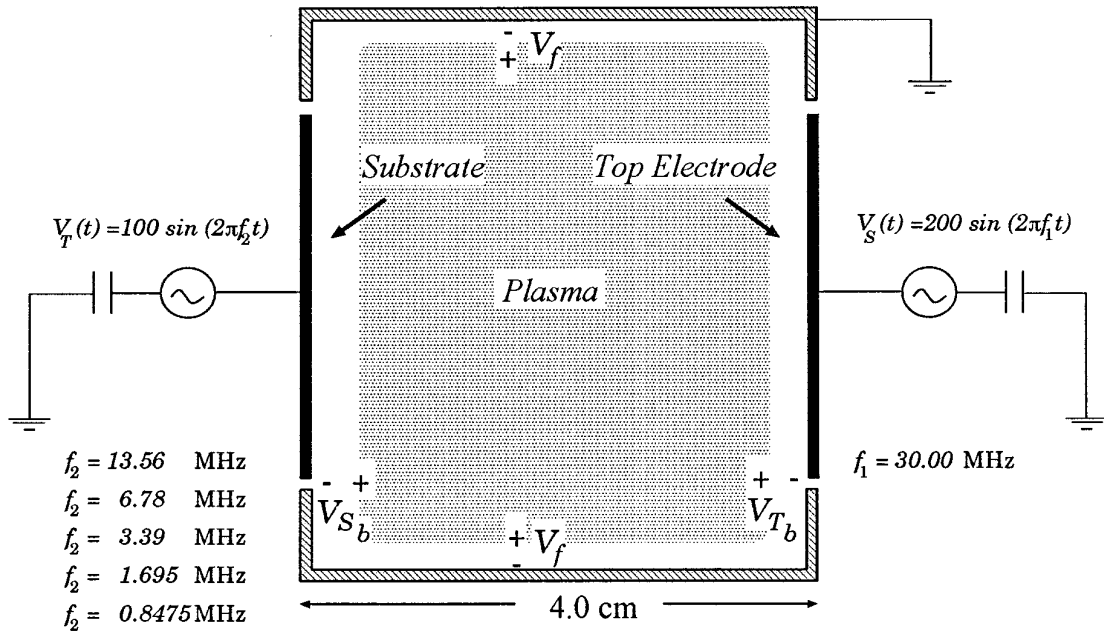
FIG. 10. Schematic of the dually excited capacitively coupled RF system. The right (source) electrode was biased at 200 V and 30 MHz, while the left (substrate) electrode was biased at 100 V at various frequencies between 1 and 13.56 MHz. All the other boundaries were grounded.
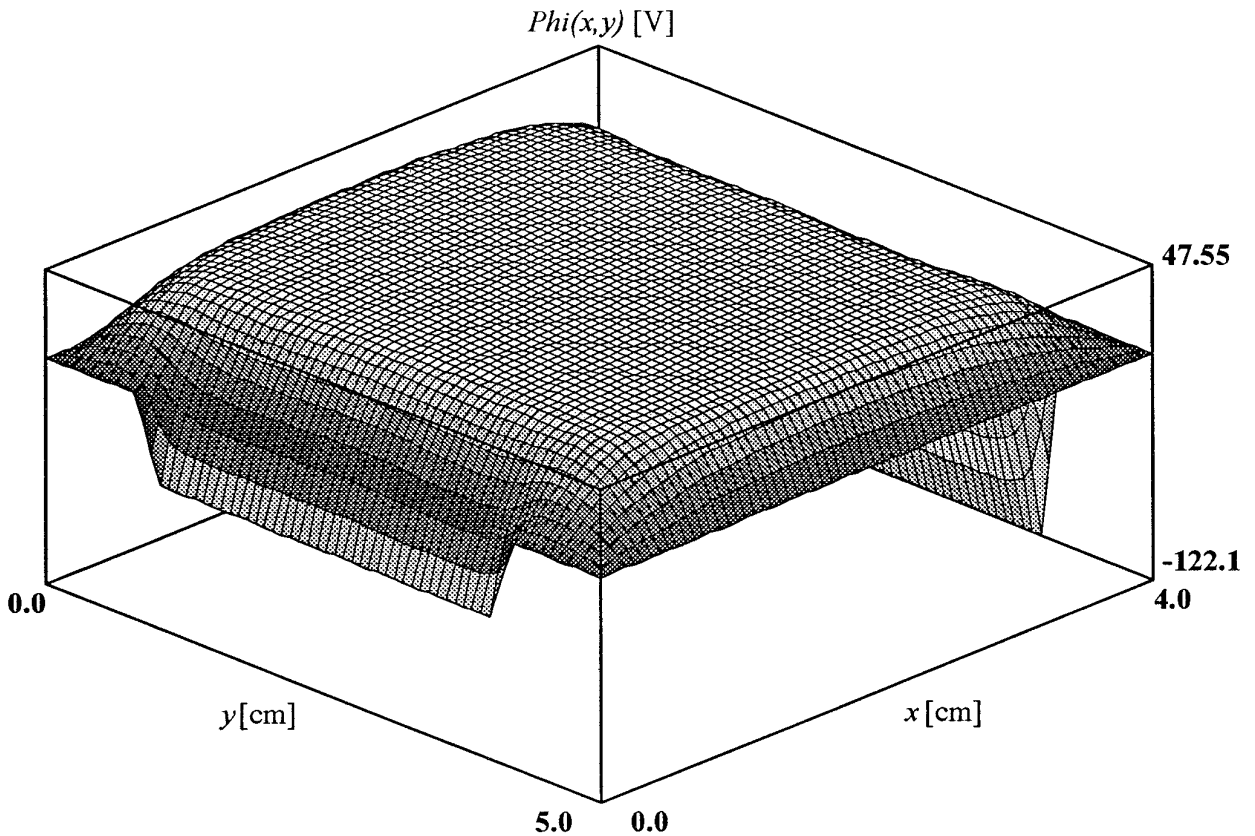

FIG. 11. Time-averaged potential in an argon plasma at $p = 10$ mTorr. The source electrode was biased at 200 V and 30 MHz, and the substrate electrode was biased at 100 V and 6.78 MHz.
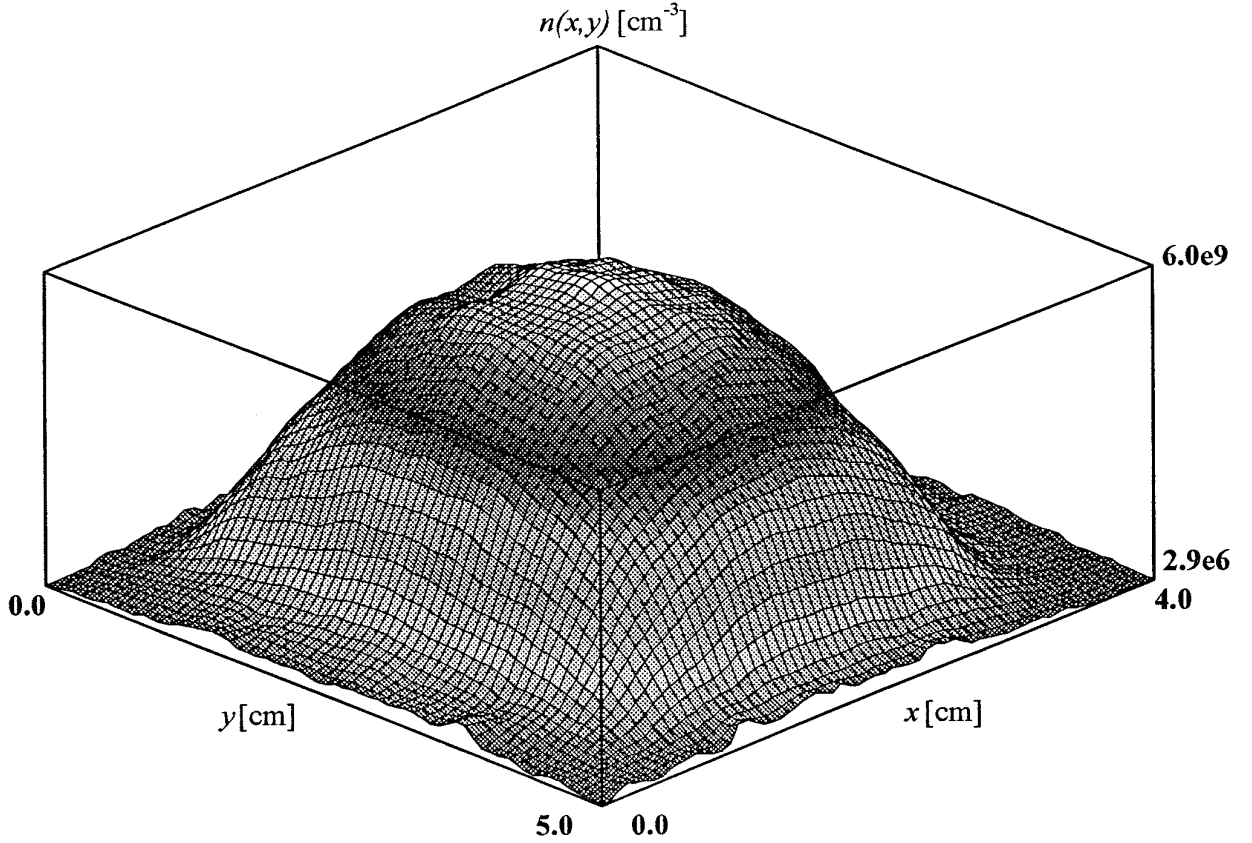
FIG. 12. Time-averaged ion density in an argon plasma at $p = 10$ mTorr. The source electrode was biased at 200 V and 30 MHz, and the substrate electrode was biased at 100 V and 6.78 MHz.

a logarithmic function of the excitation frequency. In a previous study [1], we used PDP2 to investigate the frequency scalings of various discharge parameters including plasma density n, discharge power P, and the driven sheath width s_D. At a constant bias voltage, the scalings were found to be roughly

$$P \propto n \propto \omega_0^2, \tag{37}$$

and

$$s_D \propto \frac{1}{\omega_0}. \tag{38}$$

These scalings suggest that an independent control of plasma production and ion bombarding energy may be achieved by exciting the source electrode at frequencies higher than 13.56 MHz to achieve higher densities, while the substrate electrode is biased at frequencies lower than 13.56 MHz to obtain the desired bias voltage and hence ion bombarding energy.

We used PDP2 [1, 19] to simulate a dually excited RF discharge as shown in Fig. 10. A sinusoidal voltage source of 200 V amplitude and at 30 MHz was applied to the right (source) electrode, while a similar voltage source of 100 V was applied to the left (substrate) electrode at various frequencies between 1 and 13.56 MHz. All the other boundaries were grounded. Simulations were made in an argon plasma at the gas pressure of 10 mTorr. Figure 11 shows the time-averaged potential profile in the system at the gas pressure of $p = 10$ mTorr. For the case shown in Fig. 11, the substrate was biased at 100 V and 6.78 MHz. Figure 11 shows self-biases of -45 and -122 V at the substrate and source electrodes, respectively, and a plasma potential of 48 V. Note that the time-averaged RF sheath is fully resolved. Figure 12 shows the time-averaged ion density in the system under the same conditions. The ion density is seen to peak at 6×10^9 cm^{-3}. The noise in the ion density is due to the limited number of particles used in the simulation. The noise in Fig. 12 is especially prominent in the sheath where the particle density is very low.

Figure 13 shows the substrate frequency dependence of ion density and power into the system from the substrate
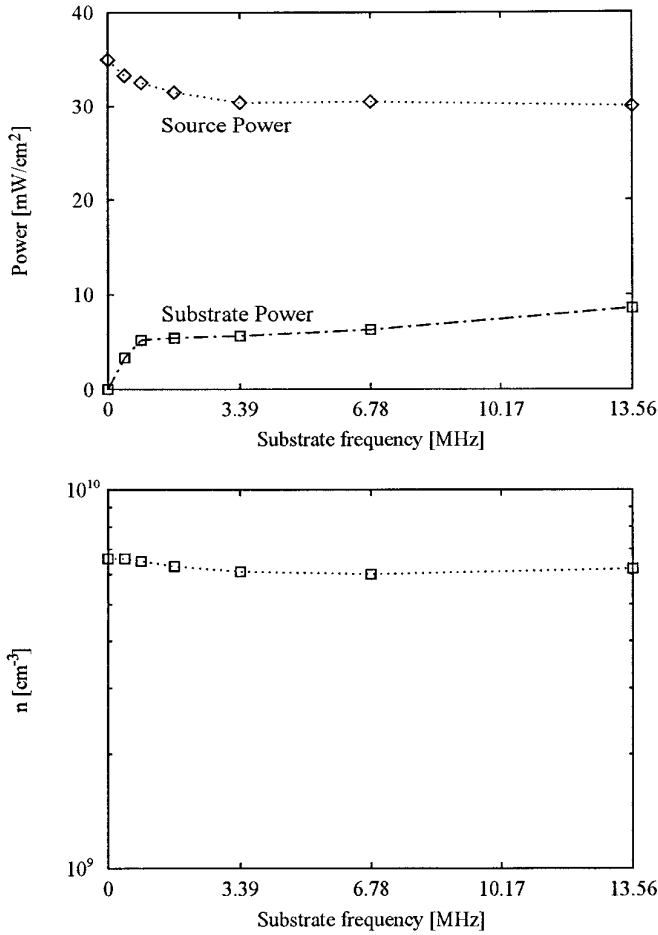
generating a high density plasma reactor with separate control over ion flux and ion bombarding energy. For the purposes of our simulations and in order to bring cases to steady state, we applied relatively low powers which resulted in lower densities than this type of source is capable of generating. Goto's measurements [29] showed that the plasma density in these discharges can reach mid to high 10^{10} cm^{-3}.

IX. CONCLUSION

We have developed an algorithm which couples external lumped circuit elements to bounded two-dimensional plasma simulation codes. This scheme allows decomposition of the field solve into a Laplace solver with boundary conditions (e.g., applied potentials) and a Poisson solver with zero boundary conditions. We presented the details of using this algorithm in both explicit and implicit codes. An explicit version of this scheme is implemented in a two-
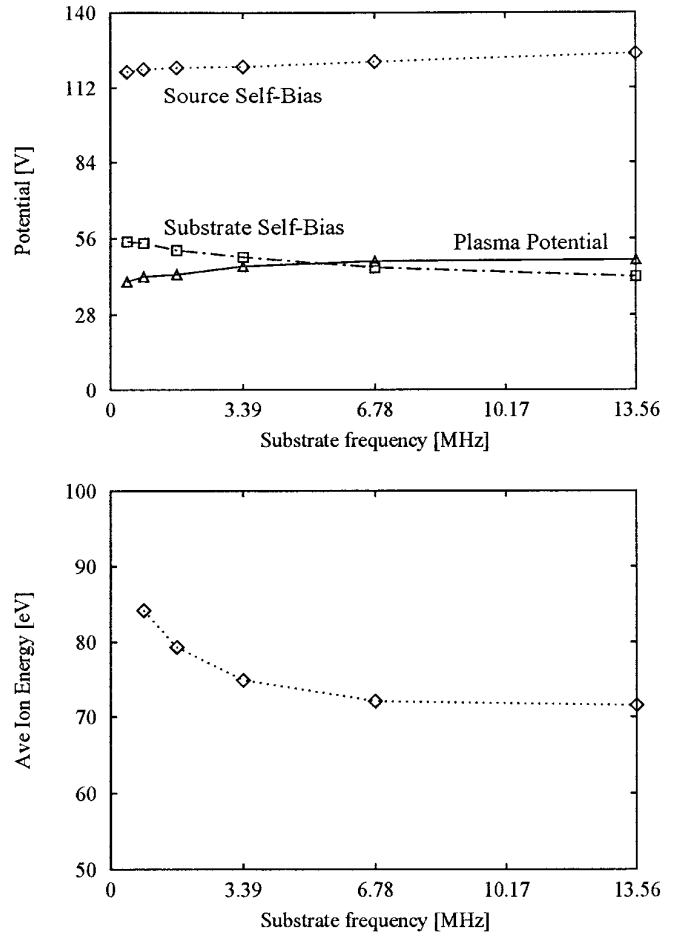
FIG. 13. The substrate frequency dependence of ion density and power into the system from the substrate and source generators at constant RF voltages.

and source generators at constant RF voltages. As the substrate frequency is increased from 0 to 13.56, the substrate power increases but stays substantially below the source power. The source power slightly decreases as the substrate frequency is raised, but stays relatively insensitive to that frequency. Hence most of the power deposited into the electrons (which results in plasma production) comes from the source electrode and is almost insensitive to the substrate frequency. As the result, the ion density shown in Fig. 13 stays relatively constant as the substrate frequency is changed.

Figure 14 shows the substrate frequency dependence of source and substrate self-biases and the average ion energy arriving at the substrate at constant RF voltages. The substrate self-bias and the average ion energy arriving at the substrate both increase as the substrate frequency is decreased which is consistent with Goto's measurements [29]. Based on the data in Figs. 13 and 14 and in Goto's measurements, it is clear that this plasma system is capable of

FIG. 14. The substrate frequency dependence of source and substrate self-biases and the average ion energy arriving at the substrate at constant RF voltages.

dimensional particle-in-cell electrostatic code called PDP2 [19]. We used PDP2 to simulate a dually excited capacitively coupled RF discharge and showed how such a system may be used as a plasma processing reactor with separate control over ion flux and ion bombarding energy.

REFERENCES

1. V. Vahedi, C. K. Birdsall, M. A. Lieberman, G. DiPeso, and T. D. Rognlien, *Phys. Fluids B* **5,** 2719 (1993).

2. M. Dalvie, M. Surendra, and G. S. Selwyn, *Appl. Phys. Lett.* **62,** 3207 (1993).

3. P. L. G. Ventzek, M. Grapperhaus, and M. J. Kushner, *J. Vac. Sci. Technol. B* **12,** 3118 (1994).

4. D. P. Lymberopoulos and D. J. Economou, *J. Vac. Sci. Technol. A* **12,** 1229 (1994).

5. R. A. Stewart, P. Vitello, D. B. Graves, and E. F. Jaeger, *Plasma Sources Sci. Technol.* **4,** 36 (1995).

6. E. F. Jaeger, L. A. Berry, J. S. Tolliver, and D. B. Batchelor, *Phys. Plasmas* **2,** 2597 (1995).

7. J. P. Verboncoeur, A. B. Langdon, and N. T. Gladd, *Comput. Phys. Comm.* **87,** 199 (1995).

8. W. S. Lawson, *J. Comput. Phys.* **80,** 253 (1989).

9. J. P. Verboncoeur, M. V. Alves, V. Vahedi, and C. K. Birdsall, *J. Comput. Phys.* **104,** 321 (1993).

10. V. A. Thomas, M. E. Jones, M. Piket-May, and A. Taflove, *IEEE Microwave Guided Wave Lett.* **4,** 141 (1994).

11. C. K. Birdsall and A. B. Langdon, *Plasma Physics Via Computer Simulation* (Hilger, Bristol, 1991).

12. J. Brackbill and B. I. Cohen, *Multiple Time Scales* (Academic Press, Orlando, 1985).

13. J. C. Adam, A. Gourdin-Serveniere, and A. B. Langdon, *J. Comput. Phys.* **47,** 229 (1982).

14. V. Vahedi and M. Surendra, *Comput. Phys. Comm.* **87,** 179 (1995).

15. M. Surendra, D. B. Graves, and I. J. Morey, *Appl. Phys. Lett.* **56,** 1022 (1990).

16. C. K. Birdsall, *IEEE Trans. Plasma Sci.* **19,** 65 (1991).

17. Y. Kaufman, *J. Phys. D* **21,** 442 (1988).

18. S. L. Lin and J. N. Bardsley, *J. Chem. Phys.* **66,** 435 (1977).

19. V. Vahedi, Modeling and simulation of RF discharges used for plasma processing, Ph.D. *Dissertation, University of California, Berkeley,* 1993. [The code PDP2 is on WWW at *http://ptsg.eecs.berkeley.edu.*]

20. A. B. Langdon and D. C. Barnes, in *Multiple Time Scales,* edited by J. Brackbill and B. I. Cohen (Academic Press, Orlando, 1985).

21. R. W. Hockney and J. W. Eastwood, *Computer Simulation Using Particles* (Hilger, Bristol, 1988).

22. S. K. Doss and K. A. Miller, *Siam. J. Numer. Anal.* **16,** 837 (1979).

23. D. W. Hewett, D. J. Larson, and S. K. Doss, *J. Comput. Phys.* **101,** 11 (1992).

24. B. I. Cohen, A. B. Langdon, and A. Friedman, *J. Comput. Phys.* **46,** 15 (1982).

25. A. B. Langdon, B. I. Cohen, and A. Friedman, *J. Comput. Phys.* **51,** 107 (1983).

26. A. Friedman, S. E. Parker, S. L. Ray, and C. K. Birdsall, *J. Comput. Phys.* **96,** 54 (1991).

27. B. I. Cohen, A. B. Langdon, D. W. Hewett, and R. J. Procassini, *J. Comput. Phys.* **81,** 151 (1989).

28. V. Vahedi, C. K. Birdsall, M. A. Lieberman, G. DiPeso, and T. D. Rognlien, *Plasma Source Sci. Technol.* **2,** 261 (1993).

29. Haruhiro H. Goto, Hans-Dirk Lowe, and Tadahiro Ohmi, *J. Vac. Sci. Technol. A* **10,** 3048 (1992).